
Bio-Inspired Self-Supervised Learning for Wrist-worn IMU Signals

Prithviraj Tarale¹ Kiet Chu¹ Abhishek Varghese¹ Kai-Chun Liu² Maxwell A Xu³ Mohit Iyyer⁴
Sunghoon I. Lee¹

Abstract

Wearable accelerometers have enabled large-scale health and wellness monitoring, yet learning robust human-activity representations has been constrained by the scarcity of labeled data. While self-supervised learning offers a potential remedy, existing approaches treat sensor streams as unstructured time series, overlooking the underlying biological structure of human movement, a factor we argue is critical for effective Human Activity Recognition (HAR). We introduce a novel tokenization strategy grounded in the *submovement theory* of motor control, which posits that continuous wrist motion is composed of superposed elementary basis functions called submovements. We define our token as the *movement segment*, a unit of motion composed of a finite sequence of submovements that is readily extractable from wrist accelerometer signals. By treating these segments as tokens, we pretrain a Transformer encoder via masked movement-segment reconstruction to model the temporal dependencies of movement segments, shifting the learning focus beyond local waveform morphology. Pretrained on the NHANES corpus ($\approx 28\text{k}$ hours; $\approx 11\text{k}$ participants; $\approx 10\text{M}$ windows), our representations outperform strong wearable SSL baselines across six subject-disjoint HAR benchmarks. Furthermore, they demonstrate stronger data efficiency in data-scarce settings. Code and pretrained weights will be made publicly available.

1. Introduction

The ubiquity of cost-effective wearable inertial sensors presents a transformative opportunity for wellness and healthcare, enabling applications ranging from fitness and

sleep tracking (Fu et al., 2020; Levy et al., 2023), remote patient monitoring (Small et al., 2019), and personalized medicine (Dunn et al., 2018). However, realizing their full potential relies on robust representations capable of recognizing human activities from raw inertial data—spanning primitive upper-limb actions like reaching-to-grasp (Wang et al., 2025), simple behaviors such as walking or sleeping (Kontaxis et al., 2024), and complex functional activities like cooking or cleaning (Shoaib et al., 2016). Unfortunately, progress in Human Activity Recognition (HAR) has been hampered by a scarcity of large-scale labeled datasets, primarily due to the prohibitive costs and labor required for annotation (Haresamudram et al., 2025).

To mitigate this label scarcity, recent research has pivoted toward developing self-supervised learning (SSL) objectives to build representations from vast volumes of unlabeled wrist-worn accelerometer data, designed to transfer effectively to limited labeled datasets (Yuan et al., 2024; Xu et al., 2025a;b). Typically, these models focus on learning features that characterize local time-series morphology within fixed-length sliding windows via unsupervised objectives, such as contrastive learning (Chen et al., 2020; Zhang et al., 2022), masked reconstruction (Narayanswamy et al., 2024), or augmentation prediction (Yuan et al., 2024). However, a fundamental limitation persists: they treat accelerometer data as unstructured time series and optimize objectives over arbitrary sample grids rather than meaningful movement units. We hypothesize that **tokenization is a key bottleneck** in wearable SSL. Without meaningful tokens, SSL tends to focus on modeling local waveform morphology and may underutilize the systematic organization of human movement. This mirrors a broader lesson from language modeling, where much of the success is enabled by pretraining on the domain’s compositional structure: meaningful tokens (words) and the syntactic rules governing their arrangement.

In this work, we bridge this gap by formalizing a bio-inspired tokenization of wrist-IMU signals, enabling sequence modeling over meaningful movement units and their temporal relations via self-supervised learning. Our approach is grounded in the *submovement theory of motor control*, which posits that continuous, complex wrist movements are constructed from the superposition of elemen-

¹College of Information and Computer Science, University of Massachusetts, Amherst, United States ²Stevens Institute of Technology, Hoboken, United States ³Google Research ⁴University of Maryland, College Park, United States. Correspondence to: Prithviraj Tarale <ptarale@umass.edu>.

tary units known as submovements (Rohrer et al., 2004). These submovements act as the fundamental building blocks of observed wrist motion, analogous to how characters or phonemes serve as the building blocks of written or spoken language. Leveraging this theoretical framework, we propose a novel token definition: the *movement segment*. Defined as a sub-second unit composed of a finite number of submovements, we posit that this segment functions as the equivalent of a “word” in natural language. The primary hypothesis of this work is that these movement segments capture useful aspects of the organizational structure of human activity, allowing the model to look beyond simple waveform morphology.

Leveraging this framework, we also introduce **Bio-PM** (Bio-inspired Tokenization-based Pretrained Model), an open pretrained encoder designed to model the temporal dependencies between movement segments. Bio-PM is pretrained on NHANES, a large-scale public wrist-IMU corpus comprising approximately 28,000 hours of data from 11,000 participants. To isolate the effect of SSL objectives, we pre-train all SSL baselines on the same corpus and evaluate them under the same subject-disjoint transfer protocol. Empirically, Bio-PM achieves the strongest performance among the controlled SSL baselines we evaluate, improving macro-F1 scores by an average of 6% (range: 4–12%) across six public HAR benchmarks. To support reproducible research, we release pretrained weights and code.

Our main contributions are:

1. **Bio-inspired Tokenization for wrist IMU.** We introduce a scalable tokenization strategy that chunks continuous accelerometer signals into meaningful movement units for sequence modeling.
2. **Contextual Representation Learning.** We present Bio-PM, a Transformer-based encoder pretrained via masked movement-segment reconstruction to capture the compositional structure of human activity.
3. **Data-efficient transfer from large-scale pretraining.** We show that segment-based pretraining improves label efficiency over SSL baselines.

2. Related Work

Self-supervised learning objectives for wearable IMU. Wearable HAR has increasingly adopted self-supervised learning to reduce reliance on labeled data (Haresamudram et al., 2022). Previous work explores three dominant families of objectives: (i) augmentation-prediction, which trains models to recognize which transformation was applied to the signal (Saeed et al., 2019; Yuan et al., 2024); (ii) masked reconstruction, which trains models to impute missing signals (Haresamudram et al., 2020; Narayanswamy et al., 2024); and (iii) contrastive learning, which encourages alignment of representations of different views of the same signal

(Chen et al., 2020; Xu et al., 2025a), including variants such as time–frequency consistency (TF-C) that align temporal and spectral views (Zhang et al., 2022).

Augmentation-prediction can work when transformations reflect realistic sensor variability, but it is sensitive to augmentation choice: artifacts or shortcuts (e.g., boundary effects from chunk-and-permute) can dominate the supervisory signal and inflate pretext-task performance. Masked reconstruction yields dense supervision from unlabeled data, but raw-value targets can often be solved via local interpolation and sensor statistics unless masking strategies and model bias force broader context use. Contrastive objectives (including TF-C) often transfer well by enforcing invariances across views, but what they learn depends strongly on view design and batch composition and can prioritize augmentation-invariant cues over finer-grained activity structure. TF-C is a particularly competitive baseline in our setting.

However, across these families, IMU signals are often treated as unstructured time series, with token boundaries chosen by arbitrary rules rather than aligned to meaningful motion events. This ignores the event-level structure of human movement, and consequently there is little pressure on models to learn that structure. Since activities are compositions of motion events, so ignoring event boundaries can limit transfer. We therefore argue that **tokenization is a missing design axis**: in this work, we study it directly by proposing a biologically motivated tokenization for wrist IMU and evaluating it under controlled conditions. Specifically, we pretrain multiple SSL objectives on the same upstream corpus and compare them using identical downstream protocols (Sec. 3); this isolates methodological differences from upstream data quality and quantity.

3. Methods

3.1. Biological Prior: The Submovement Theory

The proposed tokenization draws on the *submovement theory* of motor control (Krebs et al., 1999; Elliott et al., 2001; Rohrer et al., 2004; Hogan & Sternad, 2012; Miranda et al., 2018). The theory treats the hand/wrist as the upper-limb’s end-effector and posits that its continuous motion along each Cartesian axis can be described as a superposition of discrete bell-shaped kinematic units, called *submovements*, as illustrated in Figure 2 (right end). For axis $i \in x, y, z$, velocity is expressed as

$$v_i(t) = \sum_{k=1}^K \bar{v}_{ik} \cdot \sigma(t | \tau_k, d_k), \quad (1)$$

where K is the number of submovements. Each submovement k is defined by a normalized bell-shaped basis function $\sigma(\cdot)$ with onset τ_k , duration d_k , and peak velocity \bar{v}_{ik} .

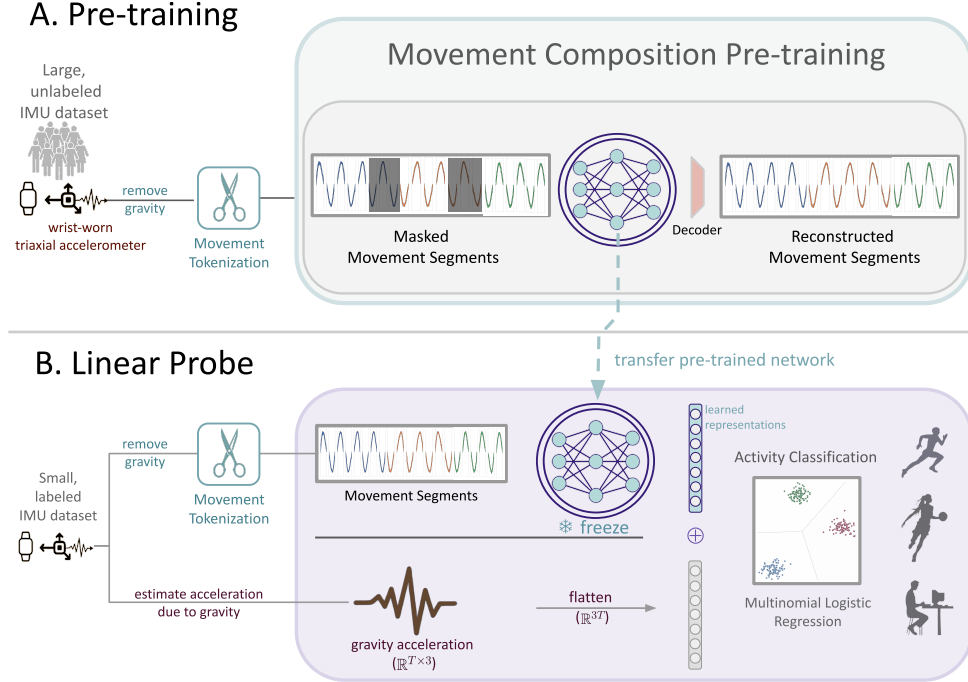


Figure 1. Bio-PM Representation Learning. We (i) tokenize accelerometry into movement-aligned segments, (ii) pretrain by modeling temporal relation across segments with a Transformer under masked reconstruction, and (iii) transfer the frozen encoder to downstream HAR for linear probing.

The canonical bell-shaped profile originates from observations of point-to-point reaching tasks—the most fundamental form of goal-directed upper-limb movement—where the hand moves between two positions, starting and ending at rest (Guigon et al., 2007). Crucially, this profile exhibits *shape invariance*: although parameters such as duration d_k and peak velocity \bar{v}_{ik} scale with movement distance and speed, the underlying normalized shape $\sigma(\cdot)$ remains constant (Flash & Hogan, 1985). Submovement theory generalizes this principle to complex behaviors, modeling continuous velocity profiles as sequences of partially overlapping submovements (Hogan & Sternad, 2012).

3.2. Proposed Tokenization of Wearable IMU Data

We seek a tokenization that captures the compositional structure of human movement described by submovement theory while remaining computationally tractable for continuous wearable accelerometer streams. Although the *submovement* is the atomic unit of upper-limb movements, using it directly as a token introduces two practical limitations. First, estimating submovement parameters in Eq. (1) requires iterative fitting procedures (Rohrer & Hogan, 2003; 2006), which are prohibitively expensive to run continuously at scale. Second, as a low-level kinematic primitive, a single submovement carries limited semantic content in isolation; we view it as analogous to a “phoneme” or a “letter” in natu-

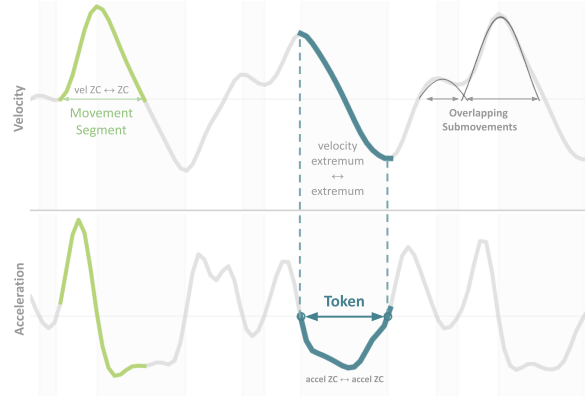


Figure 2. Movement segments in the velocity domain arise from overlapping submovements; we operationalize analogous units directly from accelerometry by defining tokens between successive acceleration Zero-Crossings (corresponding to velocity extrema). Example shown for walking (MHealth); Appendix Fig. 5 details the full tokenization pipeline.

ral language—useful for composition, but rarely meaningful alone.

We therefore adopt the *movement segment* (Daneault et al., 2023) as our guiding unit of tokenization. In the velocity domain, a movement segment is defined as the interval between successive zero-crossings of velocity, as depicted using shades in Figure 2 (left end). We posit that movement

segments, representing an initialization and termination of movements in each axis, could function as a word-like unit whose temporal organization yields higher-level contexts that a sequence model can exploit. However, directly tokenizing in the velocity domain poses significant practical hurdles for wearable accelerometry. Accelerometers measure acceleration, so velocity must be obtained by numerical integration (e.g., Simpson’s rule), increasing compute and introducing artifacts such as integration drift that degrade signal fidelity over continuous sensor streams.

To circumvent these complications, we define token boundaries at acceleration zero-crossings, formally referred to as ‘type 2’ movement segments (Simo et al., 2014; Nunes et al., 2025; Noy et al., 2025). This strategy is kinematically justified: a bell-shaped velocity profile manifests as a biphasic acceleration profile, where the peak velocity coincides precisely with a zero-crossing in acceleration. This choice is supported by clinical research, which demonstrates that the morphology and temporal organization of these segments encode critical markers of motor impairment in neurological conditions, such as stroke (Simo et al., 2014), Parkinson’s disease (Noy et al., 2025), and Huntington’s disease (Nunes et al., 2025). The fact that these specific segments are sensitive to underlying motor phenotype suggests they faithfully capture the compositional structure of human movement.

Appendix Fig. 5 provides a visual guide to our tokenization pipeline; we outline the components here and defer the formalization to Sec. 3.3. Our tokenization targets linear acceleration (voluntary motion), but raw accelerometer signals superpose both linear and gravitational components. We estimate linear acceleration by applying a 0.5 Hz high-pass filter to each axis, following standard practice in inertial sensing (Van Hees et al., 2013; Nunes et al., 2025). The resulting high-frequency component is then tokenized into movement segments by detecting zero-crossings in the filtered signal. Note that the residual low-frequency component also retains semantic value: largely due to the imperfect separation of digital filtering, it captures not only static gravity but also slow rotational movements, providing essential postural context (e.g., distinguishing sitting from lying). We describe how we re-incorporate this low-frequency component for downstream evaluation in Sec. 3.4.

3.3. Self-Supervised Pretraining Pipeline

Our goal is to learn representations of wrist IMU that capture the temporal organization of movement segments. To this end, we pretrain a segment-based Transformer encoder using a masked reconstruction objective. In this section, we describe (i) IMU windowing and movement-segment tokenization, (ii) CNN segment encoding, (iii) Transformer sequence modeling, and (iv) masked segment reconstruction.

Windowing and tokenization. We partition the gravity-reduced accelerometer stream into non-overlapping 10 s windows, $\mathcal{X}_j \in \mathbb{R}^{T \times 3}$, where j indexes windows and T is the number of samples per window. For each axis $A \in \{x, y, z\}$, we detect consecutive sign changes (zero-crossings) in $\mathcal{X}_j^{(:,A)}$ and define a movement segment as the samples between successive zero-crossings. Let $\mathcal{S}_j^{i,A}$ denote the i -th segment on axis A within window j . To suppress noise-induced crossings near zero, we apply a two-stage hysteresis (temporal and amplitude); implementation details are provided in Appendix F.2.

We resample each segment $\mathcal{S}_j^{i,A}$ to a fixed length $L=32$ using linear interpolation, yielding $\tilde{\mathcal{S}}_j^{i,A} \in \mathbb{R}^L$. We also retain segment metadata: (i) duration in samples $D_j^{i,A}$ to preserve original temporal fidelity, (ii) midpoint time $t_j^{i,A}$ within the zero-crossing-window for position encoding, and (iii) axis identifier A to preserve spatial fidelity.

Movement-segment encoder (CNN). Because the local waveform within a movement segment encodes kinematic structure (e.g. peaks, asymmetry, and oscillation rate), we apply a 1D CNN to each resampled segment $\tilde{\mathcal{S}}_j^{i,A} \in \mathbb{R}^L$ to produce an embedding $h_j^{i,A} \in \mathbb{R}^{60}$. We form the token representation by concatenating (a) the CNN embedding, (b) a learned 3-dimensional axis embedding $e(A)$, and (c) its original duration $D_j^{i,A}$ (scalar):

$$z_j^{i,A} = \left[h_j^{i,A}, e(A), D_j^{i,A} \right]. \quad (2)$$

This construction yields tokens $z_j^n \in \mathbb{R}^{64}$ (60 CNN + 3 axis + 1 duration), chosen based on upstream model size analysis (Appendix B, Table 4). We then merge tokens from all three axes and sort them by midpoint time to obtain a single token sequence $z_j^{n_{N_j}}$ for window j , where N_j is the number of segments.

Temporal reasoning (Transformer). We use a Transformer encoder to model dependencies across movement segments. Given the sequence $\{z_j^n\}_{n=1}^{N_j}$, a 5-layer Transformer encoder produces contextual embeddings $\{u_j^n\}_{n=1}^{N_j}$. Because segment timing is irregular, standard absolute/sinusoidal positional encodings—which implicitly assume roughly uniform spacing—can be unsuitable. We, therefore incorporate explicit time information through time-aware positional encodings.

Time-aware positional encodings.

Let t_j^n denote the midpoint time of token n within window j (stored as metadata), and let $\tilde{t}_j^n \in [0, 1]$ be its normalized value within the 10 s window. We encode absolute phase by

adding an MLP time embedding $p(\tilde{t}_j^n)$:

$$\tilde{z}_j^n = \text{LN}(z_j^n + p(\tilde{t}_j^n)). \quad (3)$$

For relative timing, we compute pairwise offsets $\Delta t_j^{i,k} = t_j^i - t_j^k$ and normalize by the window’s median inter-token interval. Intuitively, this approximates the number of typical inter-segment “steps” between segments i and k . We discretize the normalized offsets, index a learned relative-position embedding, and add the resulting bias to the attention logits. We include an ablation of positional information in Appendix F.1.

Masked movement-segment reconstruction. We pre-train the model by reconstructing masked movement segments from surrounding context. To encourage both local interpolation and long-range inference, we use a hybrid masking policy. For each window, we sample one of two masking schemes with equal probability: (i) random masking, which masks a fraction r of tokens at random, and (ii) contiguous time masking, which partitions the 10 s window into 1 s bins, masks a fraction r of bins, and then masks every segment that overlaps a masked bin. After CNN encoding, masked tokens are replaced with a learned [MASK] embedding. We set the masking rate to $r=0.5$, selected empirically by sweeping $r \in \{0.25, 0.50, 0.75\}$ (see Appendix Table 3).

To discourage trivial copying from visible context, we additionally corrupt visible tokens: for 20% of unmasked tokens, we replace only the CNN embeddings h with one sampled from another token from the same window, while keeping the original metadata (axis, duration, time).

A decoder reconstructs the resampled waveform \tilde{S}_j^n for each valid token. We minimize an ℓ_1 reconstruction loss over non-padding tokens, upweighting masked tokens by a factor of 100.

3.4. Downstream Embeddings

Given a window \mathcal{X}_j , the Transformer produces contextual token embeddings $\{u_j^n\}_{n=1}^{N_j}$ for the movement segments in that window. We summarize these embeddings using mean and standard-deviation pooling and concatenate them to form a window-level segment representation $T_j \in \mathbb{R}^{128}$.

Re-incorporating gravity. Because our tokenization operates on gravity-reduced acceleration, T_j does not encode static posture and device orientation. For downstream linear probing, we re-incorporate the low-frequency residual g_j by low-pass filtering the same raw acceleration stream using the matched cutoff of 0.5 Hz. We resample g_j to 300 samples per axis and vectorize it into $\text{flat}(g_j) \in \mathbb{R}^{900}$. The fused probe feature is $F_j = [T_j, \text{flat}(g_j)] \in \mathbb{R}^{1028}$. Note

that this fusion does not add additional information relative to methods that operate on raw acceleration; it simply restores the low-frequency component that is removed when forming gravity-reduced tokens.

3.5. Baselines

To isolate the effect of the SSL objective, we pretrain all baselines on the same NHANES corpus with matched windowing/sampling, and evaluate all methods under the same subject-disjoint transfer protocol. We consider four SSL objectives: (i) contrastive learning (TF-C) (Zhang et al., 2022), (ii) augmentation prediction (AugPred; replicating the architecture and objective of Yuan et al. (2024)), (iii) masked reconstruction with equal-length chunking (naive tokenization), and (iv) our masked reconstruction of movement segments. The equal-chunking baseline directly ablates tokenization: it keeps the masked-reconstruction objective fixed while replacing movement-segment tokens with equal-length chunks. Upstream training metrics for all baselines are reported in Appendix C. Additional implementation details (optimizers, model sizes, and baseline architectures) are provided in Appendix D.

We also include two generic time-series foundation models – Chronos (Ansari et al., 2024) and Moment (Goswami et al., 2024) – as contextual reference points. Note that we evaluate their publicly released checkpoints without additional pretraining.

3.6. Evaluation: Human Activity Recognition

We evaluate cross-subject generalization using *subject-disjoint* splits throughout. For datasets with ≤ 10 subjects, we use leave-one-subject-out cross-validation (LOSOCV). For datasets with > 10 subjects, we use 5-fold subject-wise cross-validation, ensuring test subjects are disjoint across folds. We report Macro-F1 on held-out test subjects as mean \pm standard deviation across splits.

Linear probing protocol. For all 10 s windows, we extract a representation using the frozen pretrained encoder. Then, for each representation and split, we (i) fit z-score normalization on the training subjects and apply it to train/test, (ii) select C by cross-validating on the training subjects to maximize Macro-F1, (iii) refit multinomial logistic regression with the selected C on all training subjects, and (iv) report Macro-F1 on held-out test subjects.

To contextualize the probe capacity, we report the number of trainable parameters in the logistic-regression classifier for each representation variant in Appendix G (Table 6).

Table 1. Macro-F1 (mean \pm std) on six subject-disjoint HAR benchmarks using frozen representations and multinomial logistic regression. All wearable SSL baselines are pretrained on the same NHANES upstream corpus under a matched transfer protocol; generic time-series foundation models are included only as contextual reference and are not pretrained on NHANES.

Model	UMH	PAMAP	WISDM	MHealth	WHARF	HAD	Avg.
<i>Generic Time Series FMs</i>							
Chronos (8.3M)	0.23 ± 0.02	0.56 ± 0.04	0.53 ± 0.02	0.63 ± 0.05	0.25 ± 0.04	0.34 ± 0.07	0.42 (n=6)
Moment (35M)	0.48 ± 0.04	0.64 ± 0.07	0.68 ± 0.03	0.66 ± 0.06	0.37 ± 0.14	0.72 ± 0.04	0.59 (n=6)
<i>Controlled (NHANES pretrained)</i>							
AugPred (Yuan et al., 2024) (10.5M)	0.29 ± 0.03	0.55 ± 0.07	0.56 ± 0.02	0.60 ± 0.08	0.24 ± 0.07	0.41 ± 0.03	0.44 (n=6)
Mask-Recon (1.4M)	0.39 ± 0.04	0.61 ± 0.05	0.58 ± 0.02	0.62 ± 0.06	0.30 ± 0.09	0.33 ± 0.07	0.47 (n=6)
Contrastive (TF-C) (8.7M)	0.53 ± 0.07	0.62 ± 0.13	0.64 ± 0.04	0.68 ± 0.17	0.37 ± 0.12	0.72 ± 0.08	0.59 (n=6)
Bio-PM (1.4M)	0.57 ± 0.05	0.69 ± 0.16	0.70 ± 0.03	0.80 ± 0.08	0.41 ± 0.03	0.75 ± 0.06	0.65 (n=6)

4. Results & Analysis

4.1. Comparing Self-Supervised Objectives

Under a controlled upstream setting where *all* SSL baselines are pretrained on the same NHANES corpus and evaluated with the same subject-disjoint linear-probe protocol, we find: (i) Bio-PM transfers best across all six HAR benchmarks (Table 1); (ii) movement-aligned tokenization is a major contributor to the gains, as replacing it with structure-agnostic equal chunking degrades transfer by **0.18 Macro-F1 on average** (Table 2); and (iii) Bio-PM is more label-efficient and **encodes order-dependent motion cues that support generalization to unseen transitions** (Fig. 4, Sec. 4.3).

4.1.1. EVALUATING TRANSFER VIA LINEAR PROBE

Table 1 reports Macro-F1 for frozen linear probes across six subject-disjoint HAR benchmarks. Bio-PM achieves the best average transfer (0.65 Macro-F1) and is best on every dataset among the compared baselines. Compared to TF-C, a strong time-series contrastive baseline, Bio-PM improves transfer *consistently* (average +0.06), with the largest margin on MHealth (+0.12; 0.80 vs. 0.68). Relative to AugPred (Yuan et al. (2024)’s methodology), Bio-PM improves by +0.21 on average, and relative to a capacity-matched masked-reconstruction baseline it improves by +0.18 on average.

4.1.2. ISOLATING TOKENIZATION STRATEGY

We isolate tokenization by keeping the pretraining objective, model capacity, optimizer, masking rate, and downstream linear-probing protocol fixed, and *only* swapping the tokenization strategy by pretraining the masked reconstruction model with uniform equal-length chunks (Table 2). For uniform chunking, we form fixed-length chunk tokens and encode them with the same CNN segment encoder used by Bio-PM (which expects a 32-sample waveform per token). We choose the chunk duration to approximately match the typical temporal support of movement-segment tokens (yielding ~ 0.5 s at 80 Hz) and resample each chunk to 32 samples, so the ablation primarily tests boundary alignment rather than changes in per-token temporal resolution.

Swapping tokenization strategy for uniform chunks reduces average Macro-F1 from 0.65 to 0.47 (**-0.18**), with the largest drops on HAD, UMA-Hand, and MHealth (Table 2). Because the objective and capacity are matched, this gap supports the interpretation that our proposed movement-aligned tokenization contributes substantially to transfer, i.e., is a task-relevant **inductive bias**.

4.1.3. ADDITIONAL ABLATIONS: GRAVITY AND PRETRAINING

Gravity (low-frequency) component. Our tokenization is applied to gravity-reduced acceleration to emphasize voluntary motion acceleration; however, the raw accelerome-

Table 2. Macro-F1 (mean \pm std) under controlled ablations isolating key design choices, including tokenization, gravity, and pretraining.

Model	UMH	PAMAP	WISDM	MHealth	WHARF	HAD	Avg.
Bio-PM	0.57 ± 0.05	0.69 ± 0.16	0.70 ± 0.03	0.80 ± 0.08	0.41 ± 0.03	0.75 ± 0.06	0.65 ± 0.07
Bio-PM w/o Gravity	0.48 ± 0.04	0.60 ± 0.04	0.67 ± 0.02	0.70 ± 0.04	0.33 ± 0.08	0.55 ± 0.05	0.56 ± 0.05
Bio-PM w/o Proposed Tokenization w. Naive Tokenization	0.38 ± 0.04	0.61 ± 0.05	0.58 ± 0.02	0.62 ± 0.06	0.30 ± 0.09	0.33 ± 0.07	0.47 ± 0.06
Bio-PM w/o Pretraining	0.45 ± 0.13	0.59 ± 0.14	0.58 ± 0.02	0.67 ± 0.12	0.41 ± 0.11	0.61 ± 0.09	0.55 ± 0.10

ter signal also contains a low-frequency orientation-related component, acceleration from gravity. Providing this component to the downstream linear probe improves average Macro-F1 from 0.56 to 0.65 (Table 2), with the largest gain on HAD (+0.20).

Interestingly, even without the low-frequency component at linear probe, Bio-PM remains strong (0.56 Macro-F1 on average) and still exceeds the uniform-chunk masked-reconstruction baseline (0.47) and AugPred (0.44) (Table 2). This further supports **movement-aligned tokenization as a strong inductive bias**.

Pretraining improves mean performance and/or stability. End-to-end finetuning the same architecture without SSL pretraining reduces average Macro-F1 (0.65 \rightarrow 0.55; Table 2). Note that end-to-end fine-tuning updates the *entire* 1.4M-parameter encoder, whereas linear probing trains only a lightweight classifier head (\sim 8k–26k parameters, depending on the dataset). Interestingly, the beneficial effect of pretraining can manifest as improved mean performance (e.g., UMH, WISDM, HAD) and/or improved reliability across splits (e.g., WHARF exhibits similar mean but substantially reduced variance after pretraining). Together, these results support that Bio-PM encodes transferable features that are difficult to recover from limited labeled data alone.

4.2. Data efficiency: Fewer subject data

In wearable HAR, recruiting and annotating diverse participant data is costly and logistically constrained. We therefore study transfer as the number of labeled training subjects decreases, which simultaneously reduces (i) subject diversity and (ii) labeled data volume. We keep the held-out test subjects fixed.

Fig. 4 shows that Bio-PM is consistently best or tied-best across subject budgets, with particularly clear improvements on MHealth and WISDM (the largest benchmark). Importantly, the relative ordering observed at full labeled-subject budgets largely persists in low-subject regimes, indicating that the improvements are not confined to high-data transfer.

4.3. Generalization to *Unseen Transitions*

Complex human behaviors are often compositional: they reuse a finite set of recurring motion units in different orders to produce diverse activities. We therefore test whether Bio-PM understands how motion units function in context by evaluating next-token prediction on *unseen* transitions.

Experimental Setup For each dataset, we first induce a discrete vocabulary by clustering token embeddings with K -means. We sweep $K \in \{16, 32, 64, 128, 256\}$ and select K by the highest silhouette score (reported in Fig. 3). This converts each 10 s window into a sequence of discrete IDs, (p_1, \dots, p_N) , where $p_i \in [1, K]$ and N represents the sequence length. We then train a *linear* classifier to predict the next token type p_{i+1} given the *frozen* embedding of the current token p_i . Most importantly, we evaluate on a *held-out bigram split*: transitions (e.g., $(A \rightarrow B)$) in the test set were excluded from the probe’s training set. This forces the model to generalize based on learned *structural* rules rather than memorized bigram frequencies.

Baselines. To isolate the source of performance, we compare Bio-PM’s contextual embeddings (post-Transformer) against: (i) Non-contextual embeddings (pre-Transformer CNN features from Eq. 2), to test the value of temporal modeling; (ii) A Markov baseline that predicts the most frequent successor observed during training; and (iii) A Shuffle control, where tokens within a window are permuted to destroy temporal ordering during training and testing.

Results. As shown in Figure 3, Bio-PM’s contextual embeddings consistently outperform the non-contextual baseline on unseen transitions across datasets (Figure 3), with improvements of +3.3 to +14.9 percentage points. Critically, shuffling token order largely removes the contextual advantage on four datasets. This failure of shuffle control implies that Bio-PM relies on the **sequential structure** and not just token-level cues. HAD is less stable in this test, as it has substantially fewer unique transitions (\sim 250 vs 2.3k–27k in the other datasets), reducing the severity of the shuffle control.

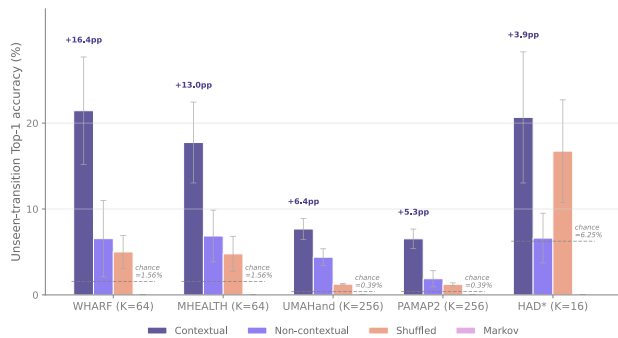


Figure 3. Next-token prediction accuracy on *unseen* token transitions using Bio-PM embeddings. Contextual embeddings outperform the non-contextual baseline, and shuffling largely removes this gain, indicating reliance on temporal organization rather than token identity alone. Chance prediction is $\frac{1}{K}$, with K selected per dataset by silhouette score. HAD* is less stable due to substantially fewer unique transitions (≈ 250 vs 2.3k–27k).

Takeaway. Bio-PM’s token embeddings reflect a token’s *function* in motion (not just its local waveform), enabling next-token prediction to generalize to unseen pairings of familiar units by leveraging function-level transition patterns.

4.4. Qualitative error analysis

We use confusion matrices to probe whether Bio-PM’s gains align with our hypothesis that movement-aligned tokens better capture activities whose labels depend on temporal phase order. We compare primarily against TF-C as the strongest controlled baseline (Appendix H). Across datasets, TF-C more often confuses classes with similar short-term motion patterns but different ordering, while Bio-PM reduces these confusions (e.g., WHARF: sit down chair 0.50 vs 0.21; lie down bed 0.17 vs 0.02; UTD-MHAD: tennis serve 0.78 vs 0.44; UMAHand: cleaning 0.80 vs 0.67). Errors remain concentrated among inherently ambiguous pairs (e.g., stair variants vs walk in wrist-only sensing), but the qualitative shifts are consistent with our unseen-transition probe (Sec. 4.3), providing converging evidence that Bio-PM better encodes order-dependent structure beyond token identity.

5. Limitations and future work

Our study demonstrates the value of movement-aligned tokenization for wrist-IMU self-supervised learning under a controlled pretraining and transfer protocol. An important open question is whether these gains persist—or widen—as upstream data and subject/sensor diversity scale (e.g., using UKBiobank). Secondly, while we focus on HAR, extending to clinical endpoints is an exciting next step, especially since submovement-based tokens have shown clinical relevance in prior studies; because these settings are high-stakes, such

evaluations would require careful study design and rigorous validation.

More broadly, we argue tokenization is a central design choice in time-series representation learning, and analogous “meaningful units” may benefit other sensor modalities.

Impact Statement

This paper advances self-supervised representation learning for wrist-worn IMU signals to improve data efficiency in human activity recognition. Our experiments use publicly available, de-identified datasets and are intended for research use on activity-recognition benchmarks. Any real-world deployment would require context-specific validation and adherence to applicable data governance and privacy practices.

References

- Ansari, A. F., Stella, L., Turkmen, C., Zhang, X., Mercado, P., Shen, H., Shchur, O., Rangapuram, S. S., Arango, S. P., Kapoor, S., Zschiegner, J., Maddix, D. C., Wang, H., Mahoney, M. W., Torkkola, K., Wilson, A. G., Bohlke-Schneider, M., and Wang, Y. Chronos: Learning the language of time series, 2024. URL <https://arxiv.org/abs/2403.07815>.
- Bai, J., Di, C., Xiao, L., Evenson, K., Lacroix, A., Crainiceanu, C., and Buchner, D. An activity index for raw accelerometry data and its comparison with other activity metrics. *PLOS ONE*, 11, 08 2016. doi: 10.1371/journal.pone.0160644.
- Banos, O., Garcia, R., Holgado-Terriza, J. A., Damas, M., Pomares, H., Rojas, I., Saez, A., and Villalonga, C. mhealthdroid: A novel framework for agile development of mobile health applications. In Pecchia, L., Chen, L. L., Nugent, C., and Bravo, J. (eds.), *Ambient Assisted Living and Daily Activities*, pp. 91–98, Cham, 2014a. Springer International Publishing. ISBN 978-3-319-13105-4.
- Banos, O., Garcia, R., and Saez, A. MHEALTH. UCI Machine Learning Repository, 2014b. DOI: <https://doi.org/10.24432/C5TW22>.
- Banos, O., Villalonga, C., Garcia, R., Saez, A., Damas, M., Holgado-Terriza, J. A., Lee, S., Pomares, H., and Rojas, I. Design, implementation and validation of a novel open framework for agile development of mobile health applications. *BioMedical Engineering OnLine*, 14(Suppl 2):S6, 2015. doi: 10.1186/1475-925X-14-S2-S6. URL <https://doi.org/10.1186/1475-925X-14-S2-S6>.
- Bruno, B., Mastrogianni, F., and Sgorbissa, A. A public

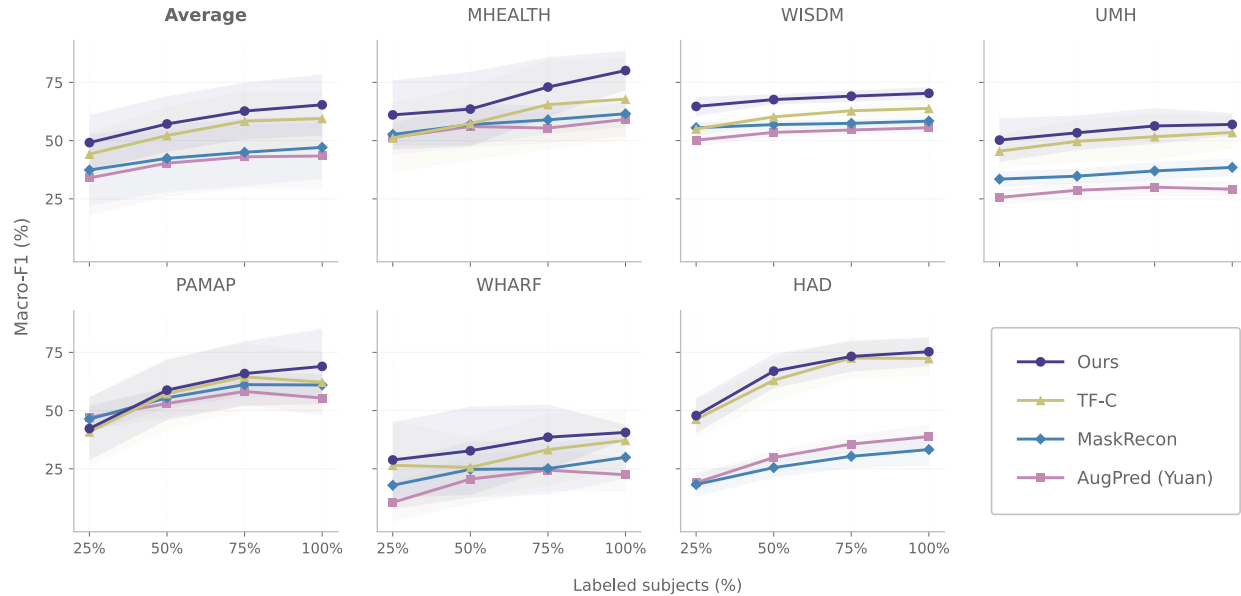


Figure 4. Macro-F1 of frozen linear probes as a function of the fraction of labeled subjects used for training (subject-disjoint splits). Bio-PM remains competitive at low label fractions and scales more favorably with additional labeled subjects than controlled SSL baselines.

domain dataset for adl recognition using wrist-placed accelerometers. In *2014 IEEE International Symposium on Robot and Human Interactive Communication (RO-MAN)*, pp. 738–743, Edinburgh, UK, 08 2014. IEEE. doi: 10.1109/ROMAN.2014.6926341.

Casilari, E., Barbosa-Galeano, J., and González-Cañete, F. J. Umahand: Hand activity dataset (universidad de máлага), 2024.

Centers for Disease Control and Prevention (CDC) and National Center for Health Statistics (NCHS). National health and nutrition examination survey data. https://wwwn.cdc.gov/Nchs/Data/Nhanes/Public/2011/DataFiles/PAX80_G_R.htm, 2011-2012. Hyattsville, MD: U.S. Department of Health and Human Services, Centers for Disease Control and Prevention.

Centers for Disease Control and Prevention (CDC) and National Center for Health Statistics (NCHS). National health and nutrition examination survey data. https://wwwn.cdc.gov/Nchs/Data/Nhanes/Public/2013/DataFiles/PAX80_H.htm, 2013-2014. Hyattsville, MD: U.S. Department of Health and Human Services, Centers for Disease Control and Prevention.

Chen, C., Jafari, R., and Kehtarnavaz, N. Utd-mhad: A multimodal dataset for human action recognition utilizing a depth camera and a wearable inertial sensor. In

2015 IEEE International Conference on Image Processing (ICIP), pp. 168–172, 2015. doi: 10.1109/ICIP.2015.7350781.

Chen, T., Kornblith, S., Norouzi, M., and Hinton, G. A simple framework for contrastive learning of visual representations, 2020. URL <https://arxiv.org/abs/2002.05709>.

Daneault, J.-F., Oubre, B., Miranda, J. G. V., and Lee, S. I. Understanding voluntary human movement variability through data-driven segmentation and clustering. *Frontiers in Human Neuroscience*, 17:1278653, 2023.

Dunn, J., Runge, R., and Snyder, M. Wearables and the medical revolution. *Personalized medicine*, 15(5):429–448, 2018.

Elliott, D., Helsen, W. F., and Chua, R. A century later: Woodworth’s (1899) two-component model of goal-directed aiming. *Psychological bulletin*, 127(3):342, 2001.

Flash, T. and Hogan, N. The coordination of arm movements: an experimentally confirmed mathematical model. *Journal of neuroscience*, 5(7):1688–1703, 1985.

Fu, B., Damer, N., Kirchbuchner, F., and Kuijper, A. Sensing technology for human activity recognition: A comprehensive survey. *IEEE Access*, 8:83791–83820, 2020. URL <https://api.semanticscholar.org/CorpusID:218579308>.

- Goswami, M., Szafer, K., Choudhry, A., Cai, Y., Li, S., and Dubrawski, A. Moment: A family of open time-series foundation models, 2024. URL <https://arxiv.org/abs/2402.03885>.
- Guigon, E., Baraduc, P., and Desmurget, M. Computational motor control: redundancy and invariance. *Journal of neurophysiology*, 97(1):331–347, 2007.
- Haresamudram, H., Tang, C. I., Suh, S., Lukowicz, P., and Ploetz, T. Past, present, and future of sensor-based human activity recognition using wearables: A surveying tutorial on a still challenging task. *Proceedings of the ACM on Interactive, Mobile, Wearable and Ubiquitous Technologies*, 9(2):1–44, 2025.
- Haresamudram, H. K., Beedu, A., Agrawal, V., Grady, P., Essa, I., Hoffman, J., and Plötz, T. Masked reconstruction based self-supervision for human activity recognition. *Proceedings of the 2020 ACM International Symposium on Wearable Computers*, 2020. URL <https://api.semanticscholar.org/CorpusID:221499205>.
- Haresamudram, H. K., Essa, I., and Plotz, T. Assessing the state of self-supervised human activity recognition using wearables. *Proceedings of the ACM on Interactive, Mobile, Wearable and Ubiquitous Technologies*, 6:1 – 47, 2022. URL <https://api.semanticscholar.org/CorpusID:247158005>.
- Hogan, N. and Sternad, D. Dynamic primitives of motor behavior. *Biological cybernetics*, 106(11):727–739, 2012.
- Kontaxis, S., Kanellos, F., Ntanis, A., Kostikis, N., Konitsiotis, S., and Rigas, G. An inertial-based wearable system for monitoring vital signs during sleep. *Sensors*, 24(13), 2024. ISSN 1424-8220. doi: 10.3390/s24134139. URL <https://www.mdpi.com/1424-8220/24/13/4139>.
- Krebs, H. I., Aisen, M. L., Volpe, B. T., and Hogan, N. Quantization of continuous arm movements in humans with brain injury. *Proceedings of the National Academy of Sciences*, 96(8):4645–4649, 1999.
- Langley, P. Crafting papers on machine learning. In Langley, P. (ed.), *Proceedings of the 17th International Conference on Machine Learning (ICML 2000)*, pp. 1207–1216, Stanford, CA, 2000. Morgan Kaufmann.
- Levy, J., Álvarez, D., Del Campo, F., and Behar, J. A. Deep learning for obstructive sleep apnea diagnosis based on single channel oximetry. *Nature Communications*, 14(1): 4881, 2023.
- Miranda, J. G. V., Daneault, J.-F., Vergara-Diaz, G., Torres, Â. F. S. d. O. e., Quixada, A. P., Fonseca, M. d. L., Vieira, J. P. B. C., dos Santos, V. S., da Figueiredo, T. C., Pinto, E. B., et al. Complex upper-limb movements are generated by combining motor primitives that scale with the movement size. *Scientific reports*, 8(1):12918, 2018.
- Narayanswamy, G., Liu, X., Ayush, K., Yang, Y., Xu, X., Liao, S., Garrison, J., Taylor, S., Sunshine, J., Liu, Y., Althoff, T., Narayanan, S., Kohli, P., Zhan, J., Malhotra, M., Patel, S., Abdel-Ghaffar, S., and McDuff, D. Scaling wearable foundation models, 2024. URL <https://arxiv.org/abs/2410.13638>.
- Noy, L., Hassin-Baer, S., Fay-Karmon, T., Kattouf, N., Israeli-Korn, S., van der Wel, R., and Friedman, J. Submovements in manual tracking: people with parkinson’s disease produce more submovements than age-matched controls. *Journal of neuroengineering and rehabilitation*, 22(1):51, 2025.
- Nunes, A. S., Yıldız Potter, İ., Mishra, R. K., Casado, J., Dana, N., Geronimo, A., Tarolli, C. G., Schneider, R. B., Dorsey, E. R., Adams, J. L., et al. Using wearable sensors and machine learning to assess upper limb function in huntington’s disease. *Communications Medicine*, 5(1): 50, 2025.
- Reiss, A. PAMAP2 Physical Activity Monitoring. UCI Machine Learning Repository, 2012. DOI: <https://doi.org/10.24432/C5NW2H>.
- Rohrer, B. and Hogan, N. Avoiding spurious submovement decompositions: a globally optimal algorithm. *Biological cybernetics*, 89(3):190–199, 2003.
- Rohrer, B. and Hogan, N. Avoiding spurious submovement decompositions ii: a scattershot algorithm. *Biological cybernetics*, 94(5):409–414, 2006.
- Rohrer, B., Fasoli, S., Krebs, H. I., Volpe, B., Frontera, W. R., Stein, J., and Hogan, N. Submovements grow larger, fewer, and more blended during stroke recovery. *Motor control*, 8(4):472–483, 2004.
- Saeed, A., Ozcelebi, T., and Lukkien, J. Multi-task self-supervised learning for human activity detection. *CoRR*, abs/1907.11879, 2019. URL <http://arxiv.org/abs/1907.11879>.
- Shoab, M., Bosch, S., Incel, O. D., Scholten, H., and Havinga, P. J. M. Complex human activity recognition using smartphone and wrist-worn motion sensors. *Sensors*, 16(4):426, 2016. ISSN 1424-8220. doi: 10.3390/s16040426. URL <https://pubmed.ncbi.nlm.nih.gov/27023543>.

- Simo, L. S., Piovesan, D., Laczko, J., Ghez, C., and Scheidt, R. S. Submovements during reaching movements after stroke. In *2014 36th Annual International Conference of the IEEE Engineering in Medicine and Biology Society*, pp. 5357–5360. IEEE, 2014.
- Small, S. R., Bullock, G. S., Khalid, S., Barker, K., Trivella, M., and Price, A. J. Current clinical utilisation of wearable motion sensors for the assessment of outcome following knee arthroplasty: a scoping review. *BMJ open*, 9(12):e033832, 2019.
- Van Hees, V. T., Gorzelniak, L., Dean León, E. C., Eder, M., Pias, M., Taherian, S., Ekelund, U., Renström, F., Franks, P. W., Horsch, A., et al. Separating movement and gravity components in an acceleration signal and implications for the assessment of human daily physical activity. *PLoS one*, 8(4):e61691, 2013.
- Wang, R., Lang, C. E., Stoykov, M. E., Bonato, P., and Lee, S. I. Wearable-based digital biomarker provides a valid alternative to traditional clinical measures for post-stroke upper-limb motor recovery. *medRxiv*, pp. 2025–01, 2025.
- Weiss, G. WISDM Smartphone and Smartwatch Activity and Biometrics Dataset . UCI Machine Learning Repository, 2019. DOI: <https://doi.org/10.24432/C5HK59>.
- Xu, M. A., Narain, J., Darnell, G., Hallgrímsson, H. T., Jeong, H., Forde, D., Fineman, R. A., Raghuram, K. J., Rehg, J. M., and Ren, S. Y. Relcon: Relative contrastive learning for a motion foundation model for wearable data. In *The Thirteenth International Conference on Learning Representations, 2025a*. URL <https://openreview.net/forum?id=k2uUeLCrQq>.
- Xu, M. A., Narayanswamy, G., Ayush, K., Spathis, D., Liao, S., Tailor, S., Metwally, A. A., Heydari, A. A., Zhang, Y., Garrison, J., Abdel-Ghaffar, S., Xu, X., Gu, K., Sunshine, J., Poh, M.-Z., Liu, Y., Althoff, T., Narayanan, S., Kohli, P., Malhotra, M., Patel, S. N., Yang, Y., Rehg, J. M., Liu, X., and McDuff, D. Lsm-2: Learning from incomplete wearable sensor data. *ArXiv*, abs/2506.05321, 2025b. URL <https://api.semanticscholar.org/CorpusID:279244242>.
- Yuan, H., Chan, S., Creagh, A. P., Tong, C., Acquah, A., Clifton, D. A., and Doherty, A. Self-supervised learning for human activity recognition using 700,000 person-days of wearable data. *npj Digital Medicine*, 7(1), April 2024. ISSN 2398-6352. doi: 10.1038/s41746-024-01062-3. URL <http://dx.doi.org/10.1038/s41746-024-01062-3>.
- Zhang, X., Zhao, Z., Tsiligkaridis, T., and Zitnik, M. Self-supervised contrastive pre-training for time series via time-frequency consistency. *ArXiv*, abs/2206.08496, 2022. URL <https://api.semanticscholar.org/CorpusID:249848167>.

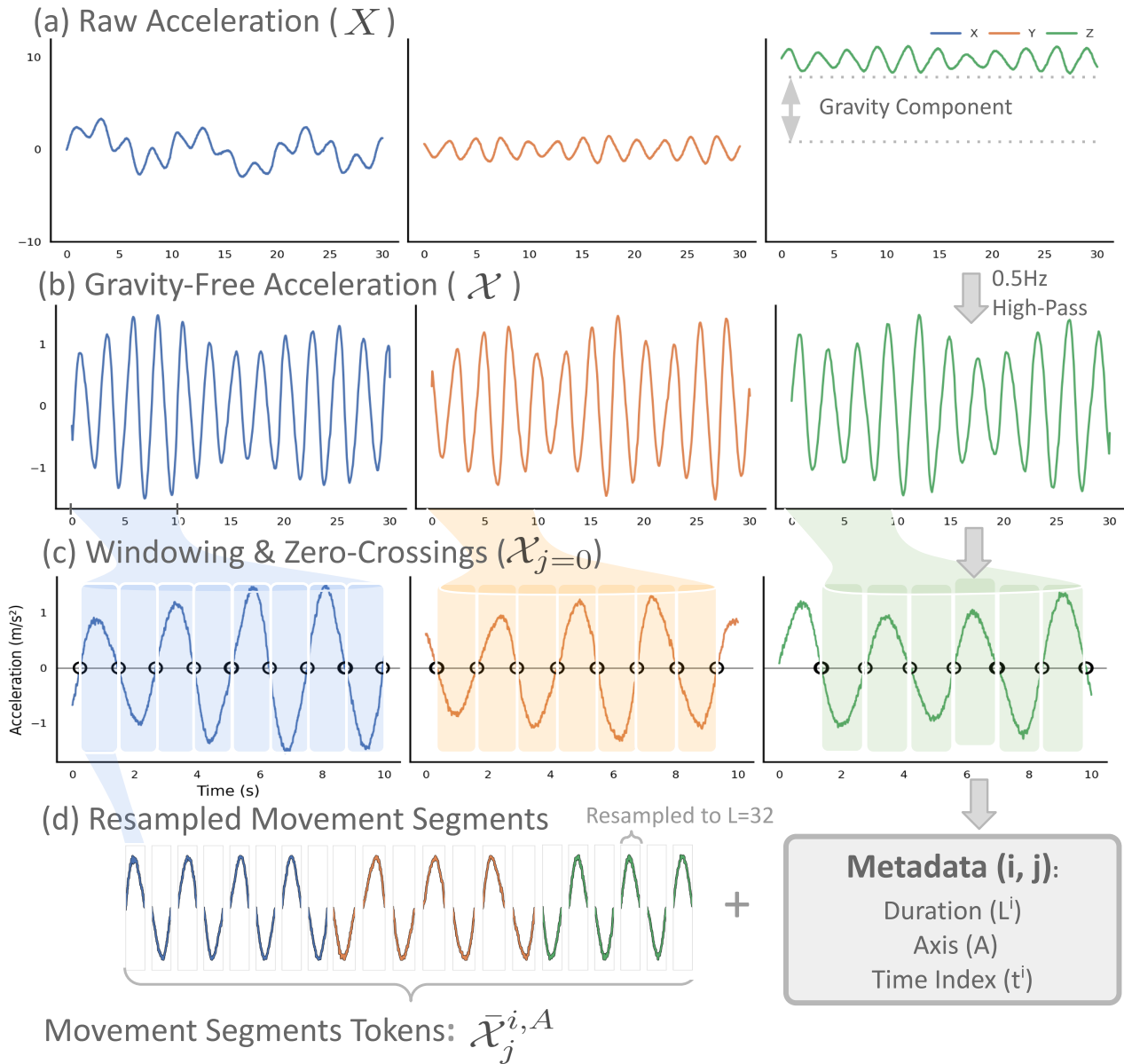
A. Tokenization Pipeline


Figure 5. End-to-end conversion from raw wrist accelerometer signals to fixed-length movement-segment tokens: gravity separation via filtering, zero-crossing boundary detection, segmentation, and resampling to a common token length, along with token metadata used for sequence modeling.

B. Our Model: Upstream Analysis

B.0.1. VARYING UPSTREAM MASKING RATE

See table 3. We chose the model pretrained on masking rate 50%.

Table 3. Effect of masking rate on linear-probe Macro-F1 for Bio-PM

Masking Rate	PAMAP	MHealth	WHARF	HAD	Avg
25%	0.69 ± 0.12	0.80 ± 0.08	0.40 ± 0.02	0.71 ± 0.06	0.65 (n=4)
50%	0.71 ± 0.12	0.80 ± 0.08	0.42 ± 0.03	0.73 ± 0.06	0.67 (n=4)
75%	0.69 ± 0.13	0.79 ± 0.10	0.41 ± 0.05	0.71 ± 0.07	0.65 (n=4)

B.0.2. VARYING MODEL SIZE.

We evaluated whether increasing Bio-PM capacity improves transfer under our largest upstream setting (11k subjects). Across downstream HAR benchmarks, scaling from 1.4M to 6M and 13M parameters yields small consistent gains in linear-probe Macro-F1 (Table 4). However, we use the 1.4M model throughout for three practical reasons: (i) it is the only configuration whose embedding dimension is closest to the Yuan et al.’s ResNet baseline (1.4M: 1028-d; 6M: 1156-d; 13M: 1412-d; ResNet: 1024-d), avoiding improvements attributable to a higher-dimensional probe space; (ii) HAR is commonly deployed on-device, making smaller backbones more suitable for edge inference; and (iii) it substantially reduced training cost and enabled broader ablations internally, while still outperforming prior methods in our main comparisons.

Concretely, the 1.4M model uses width $D=64$ with 5 Transformer layers, while the 6M and 13M variants use $D=128$ and $D=256$ respectively, each with 10 layers.

Table 4. Effect of model size on linear-probe Macro-F1 for Bio-PM

Model Size	PAMAP	MHealth	WHARF	HAD	Avg
1.4M	0.71 ± 0.12	0.80 ± 0.08	0.42 ± 0.03	0.73 ± 0.06	0.67 (n=4)
6M	0.69 ± 0.13	0.82 ± 0.1	0.43 ± 0.05	0.71 ± 0.08	0.66 (n=4)
13M	0.69 ± 0.13	0.82 ± 0.09	0.44 ± 0.05	0.76 ± 0.04	0.68 (n=4)

B.0.3. UPSTREAM DATA SAMPLING

To efficiently sample informative segments from long, free-living NHANES wrist accelerometer recordings, we use an activity-index–driven window selection strategy inspired by the Activity Index (AI) of Bai *et al.* (Bai *et al.*, 2016). Continuous streams are segmented into non-overlapping 10s windows, and each window is assigned a scalar activity score following the AI formulation. Windows with low activity ($AI < 50$) are discarded to remove near-stationary behavior that dominates free-living data. The remaining windows are stratified by activity intensity: household and moderate-intensity activities are subsampled due to their high prevalence, while all high-intensity activity windows are retained given their relative scarcity. This yields a compact yet diverse training set spanning a range of movement intensities.

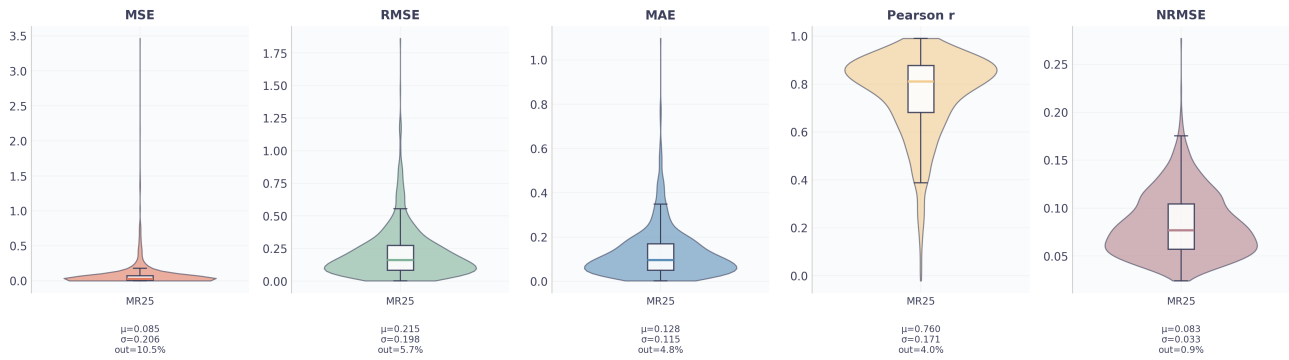
B.0.4. UPSTREAM: RECONSTRUCTION PERFORMANCE

For upstream metrics by masking rate, see Figure 6. For examples of reconstruction, see Figure 7.

C. Baseline Upstream Performances

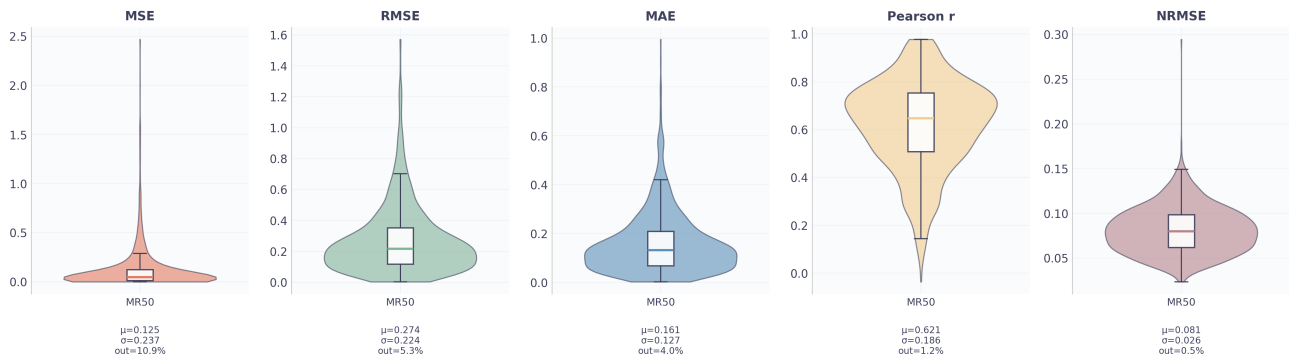
AugPred. Pretext accuracies: permutation 89.5%, time reversal 89.2%, and time warp 95.8% (comparable to the converged values reported by Yuan *et al.* (2024)).

Reconstruction Metrics — Masked Regions



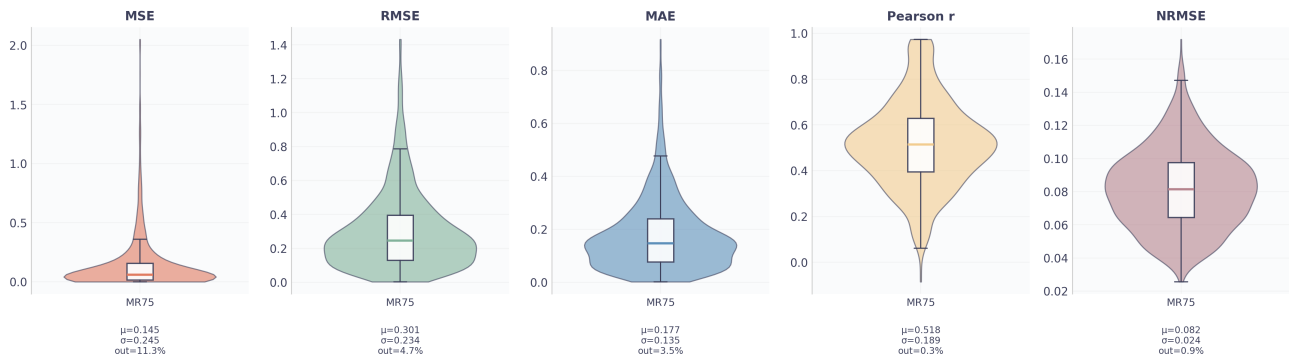
(a) MR25

Reconstruction Metrics — Masked Regions



(b) MR50

Reconstruction Metrics — Masked Regions



(c) MR75

Figure 6. Upstream masked-region reconstruction quality under different masking rates. Violin plots show the distribution of reconstruction performance evaluated only on masked regions for MR25/50/75 using MSE, RMSE, MAE, Pearson r , and NRMSE. Boxes indicate median and interquartile range (whiskers: $1.5 \times \text{IQR}$). Numbers below each subplot report mean μ , standard deviation σ , and outlier fraction. Increasing masking increases error (MSE 0.085 \rightarrow 0.145, MAE 0.128 \rightarrow 0.177) and reduces correlation ($r = 0.760 \rightarrow 0.518$), while NRMSE stays roughly constant ($\approx 0.081\text{--}0.083$).

TF-C. Validation contrastive losses: $L_{tt}=5.4298$, $L_{ff}=5.4208$, $L_{tf}=4.8183$ (total 15.6689).

Masked reconstruction (equal-chunk). Masked-token MAE: 0.35.

For each baseline, we select the checkpoint that maximizes validation Macro-F1 under the linear-probing protocol. Additional training for TF-C led to degraded validation upstream performance.

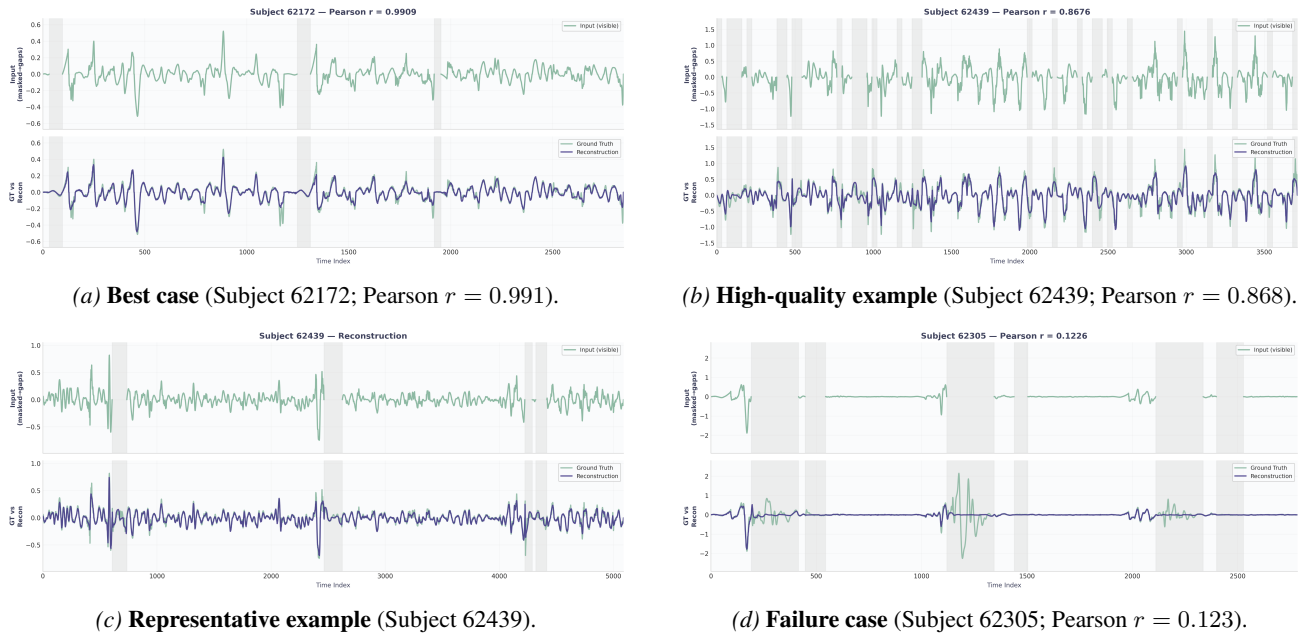


Figure 7. **Qualitative masked-region reconstruction examples.** Each panel visualizes the masked-imputation pretraining task on a representative 1D channel: the *top* subplot shows the input with masked spans removed (gray bands denote masked regions), and the *bottom* subplot overlays the ground-truth signal with the model reconstruction. Pearson r (shown in titles where available) summarizes agreement between reconstruction and ground truth on masked regions. These examples illustrate the range of outcomes from near-perfect recovery (e.g., $r \approx 0.99$) to clear failure modes ($r \approx 0.12$), where the model under-reconstructs sharp transients and high-amplitude bursts within masked segments.

D. Implementation Details

Training setup. Unless otherwise stated, all models are implemented in PyTorch. We pretrain all SSL methods on the same NHANES corpus with matched windowing and sampling.

Masked reconstruction baselines (capacity-matched). For masked reconstruction, our method and the equal-chunk baseline use the same Transformer-based architecture and identical optimization settings (Adam, learning rate 10^{-4} , batch size 512). This isolates the effect of tokenization while holding objective, optimizer, and model capacity fixed.

AugPred replication (Yuan et al.). For AugPred, we replicate the objective and augmentation pipeline of Yuan et al. (2024) and use the same backbone architecture as in their work: an 18-layer ResNet-V2 with 1D convolutions (approximately 10M parameters), producing a 1024-dimensional representation.

We follow Yuan et al. (2024) with two small implementation adjustments for our matched-upstream setting—retaining 80 Hz (no 40 Hz downsampling) and omitting weighted sampling due to our existing upstream filtering (see Sec. B.0.3). Nevertheless, we get comparable pretext accuracies as reported by Yuan et al. (2024) (Appendix C).

TF-C architecture and parameter budgeting. TF-C uses two encoders (temporal and frequency branches). To keep the total parameter budget comparable to the single-encoder baselines, we reduce the per-encoder width such that the combined TF-C model has approximately 8.4M parameters.

Bio-PM model size. Our default Bio-PM model has approximately 1.4M parameters. We also experimented with larger variants (e.g., 6M and 13M parameters) and observed similar downstream trends; we report the 1.4M model to prioritize efficiency and practical deployment considerations.

Table 5. Summary of downstream HAR datasets.

Dataset	Setting	#Sub	#Classes	Hz	References
NHANES IMU	Free-living	$\approx 11k$	–	80	(CDC & NCHS, 2011-2012; CDC & NCHS, 2013-2014)
UMH	Semi-natural	25	29	100	(Casilari et al., 2024)
PAMAP2	Lab protocol	8	8	100	(Reiss, 2012)
WISDM (Actitracker)	Semi-natural	51	18	20	(Weiss, 2019)
MHealth	Scripted protocol	10	11	50	(Banos et al., 2014b;a; 2015)
WHARF	In-home scripted	17	14	32	(Bruno et al., 2014)
UTD-MHAD	Lab multimodal	8	27	50	(Chen et al., 2015)

E. Datasets and Preprocessing

Wrist-only sensor. For multi-sensor datasets, we retain only the wrist/hand accelerometer stream and discard other body locations/modalities.

Filtering We compute (i) voluntary acceleration using a 6th-order Butterworth highpass filter (0.5Hz), and (ii) gravity using a 6th-order Butterworth low-pass filter (cutoff 0.5 Hz).

Unit normalization. All datasets were converted from m/s^2 to g (divide by 9.80665).

Labeling. For each 10s window, labels are assigned by majority vote within each window; windows dominated by transition/unknown labels are discarded.

Resampling. To ensure a consistent temporal resolution across datasets, all accelerometer signals are resampled to a common sampling rate using interpolation-based resampling. This step standardizes window lengths and frequency content across subjects and recording setups.

Windowing. The preprocessed signals are segmented into fixed-length sliding windows of 10 s with overlap. Windowing enables learning from short, locally stationary motion segments while increasing the effective number of training samples.

Quality control. Windows containing insufficient valid samples or dominated by null, transition, or excluded activity labels are removed. This filtering step reduces label noise and ensures that retained windows represent coherent activities.

Motion magnitude normalization. For each window, motion intensity is characterized using the mean absolute deviation (MAD) of the filtered acceleration magnitude. This statistic provides a robust, scale-invariant measure of movement variability and is used for downstream analysis and dataset characterization.

F. Miscellaneous

F.1. Sanity Checks and Ablations

Experiments conducted on all datasets except WISDM because of its size.

Does the transformer use temporal information? As a sanity check, we ablate positional information *at transfer time* by disabling positional encodings in the frozen pretrained encoder and retraining only the linear probe. Removing positional encodings reduces Macro-F1 by ≈ 3 points on average, with the largest drop on HAD (8.2 points). This suggests that the learned representations exploit token timing in addition to token content, particularly for order-dependent activities.

F.2. Zero-crossing hysteresis for movement-segment extraction

We extract candidate segment boundaries as sign changes in the 1D gravity-free acceleration signal. To reduce noise-induced crossings when the signal hovers near zero, we apply two heuristics:

Bio-Inspired Self-Supervised Learning for Wrist-worn IMU

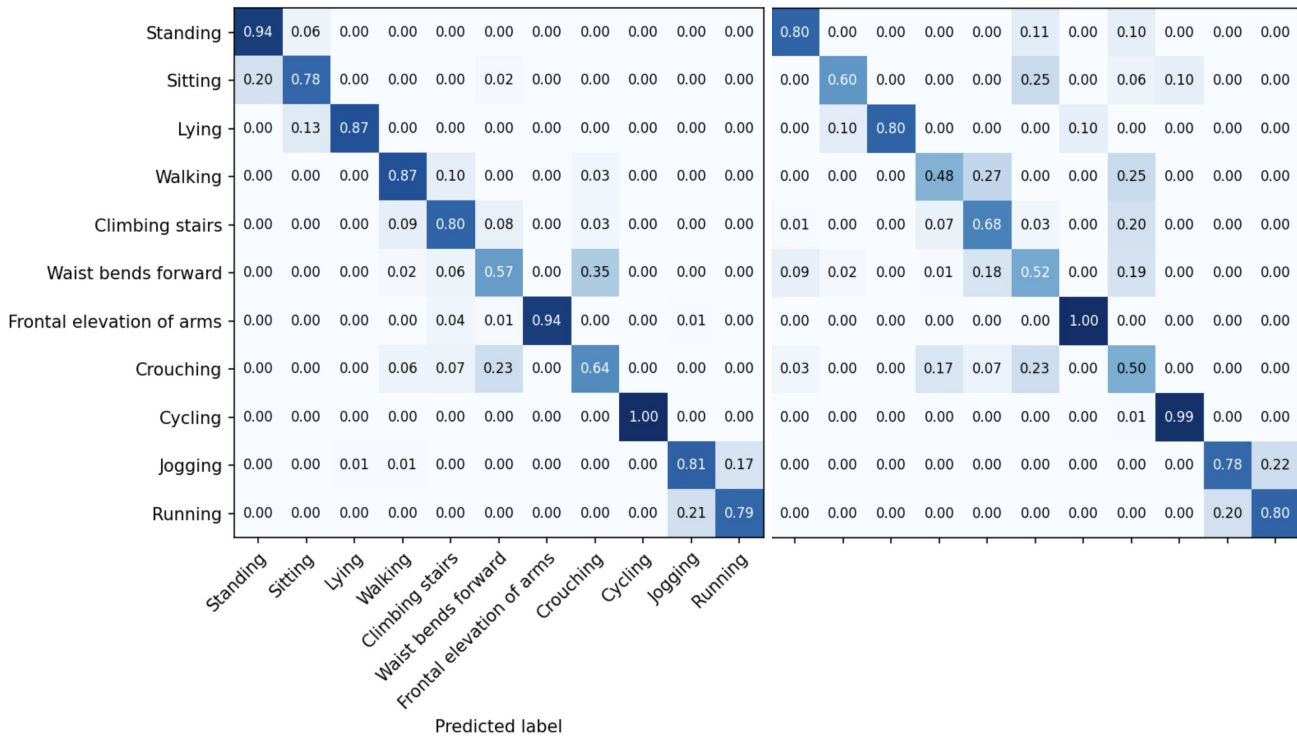


Figure 8. Bio-PM vs TF-C on Mhealth.

Temporal hysteresis. Enforce a minimum inter-crossing interval of 50 ms. Candidate crossings within 50 ms of the last accepted crossing are discarded.

Amplitude hysteresis. For each provisional segment \mathcal{S} between consecutive accepted crossings, compute peak amplitude $\max_{t \in \mathcal{S}} |x(t)|$. If two consecutive segments both have peak amplitude below 0.01, we remove their intermediate crossing and merge the two segments.

After hysteresis, each segment is resampled to a fixed length $L=32$ via linear interpolation.

G. Linear Probing Parameter Comparison

Table 6. Number of learned parameters in linear probing. Only logistic regression weights are trained; encoder weights remain frozen.

Dataset	Classes (K)	AugPred (1024-d)	TF-C (512-d)	Transformer (128-d)	Bio-PM (1028-d)
UMH	29	29,725	14,877	3,741	29,841
PAMAP2	8	8,200	4,104	1,032	8,232
MHEALTH	11	11,275	5,643	1,419	11,319
MHAD	27	27,675	13,851	3,483	27,783

H. Confusion Matrices

Bio-Inspired Self-Supervised Learning for Wrist-worn IMU

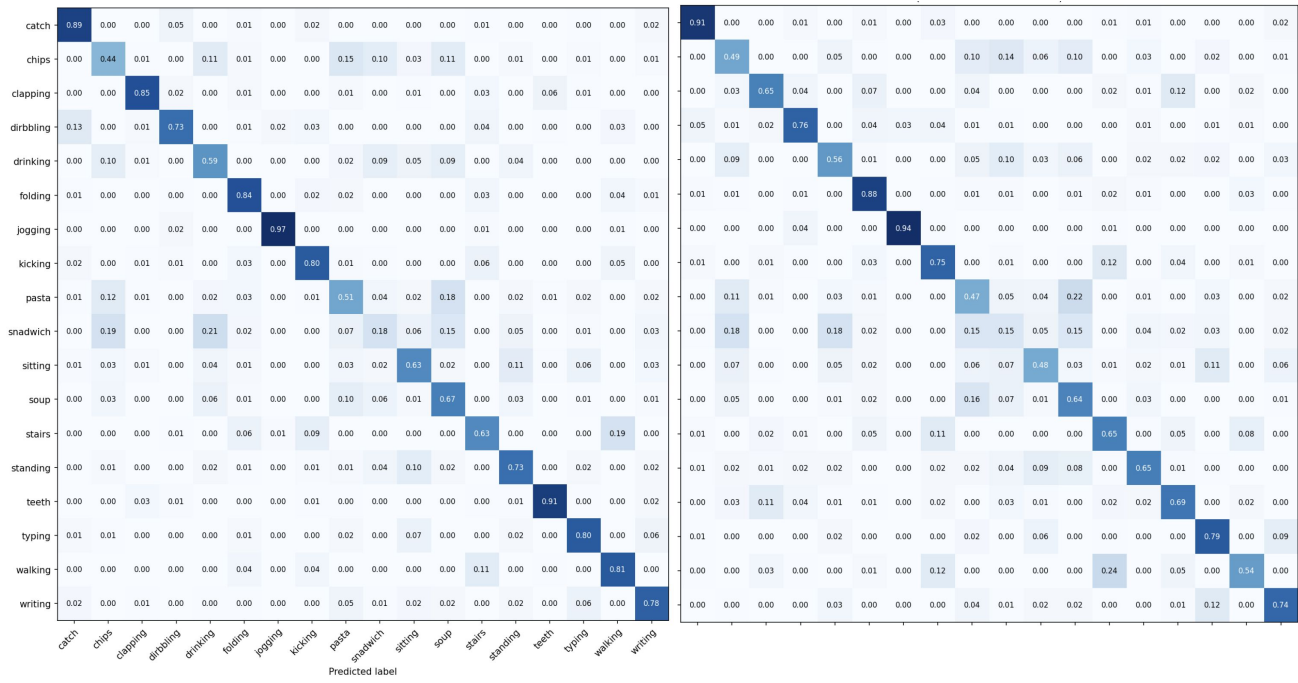
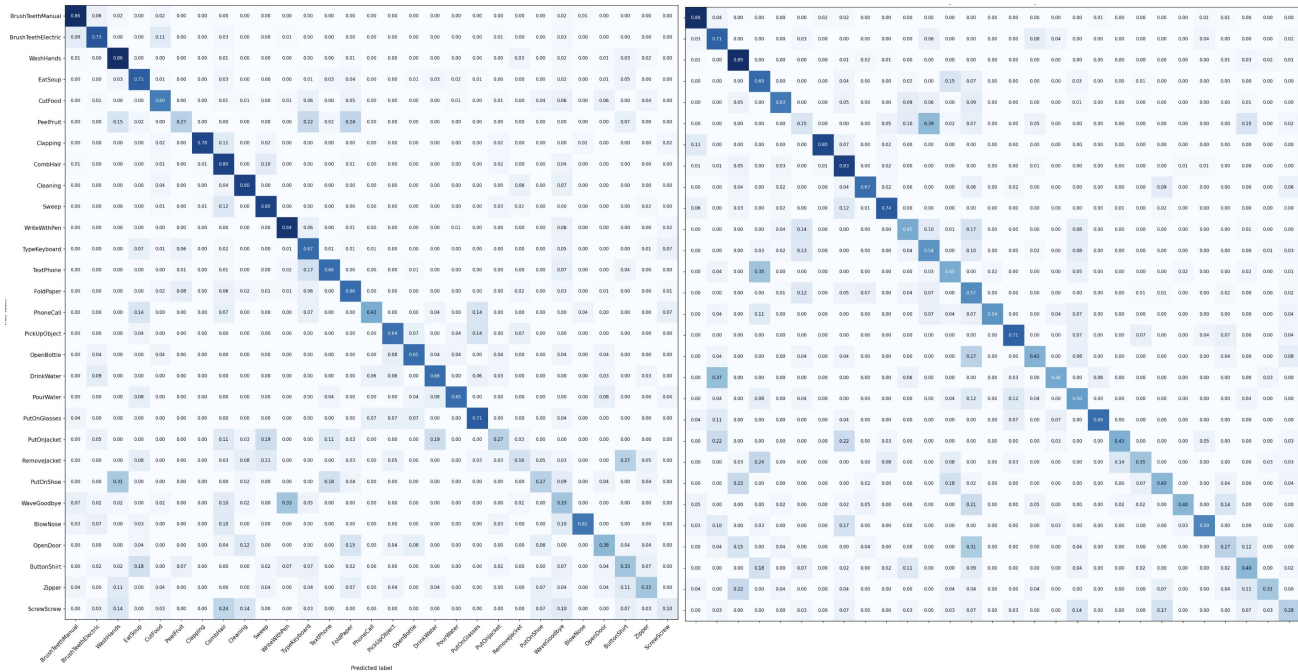


Figure 9. Bio-PM vs TF-C on WISDM.



Bio-Inspired Self-Supervised Learning for Wrist-worn IMU

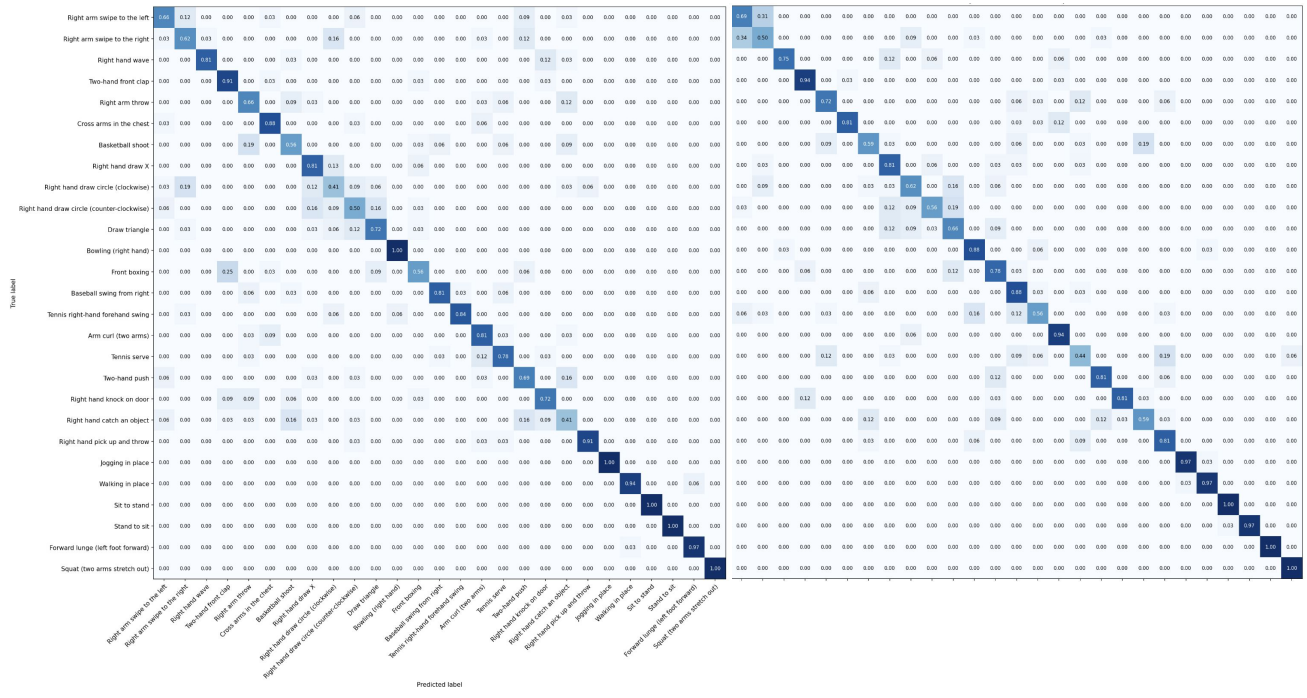


Figure 11. Bio-PM vs TF-C on HAD.

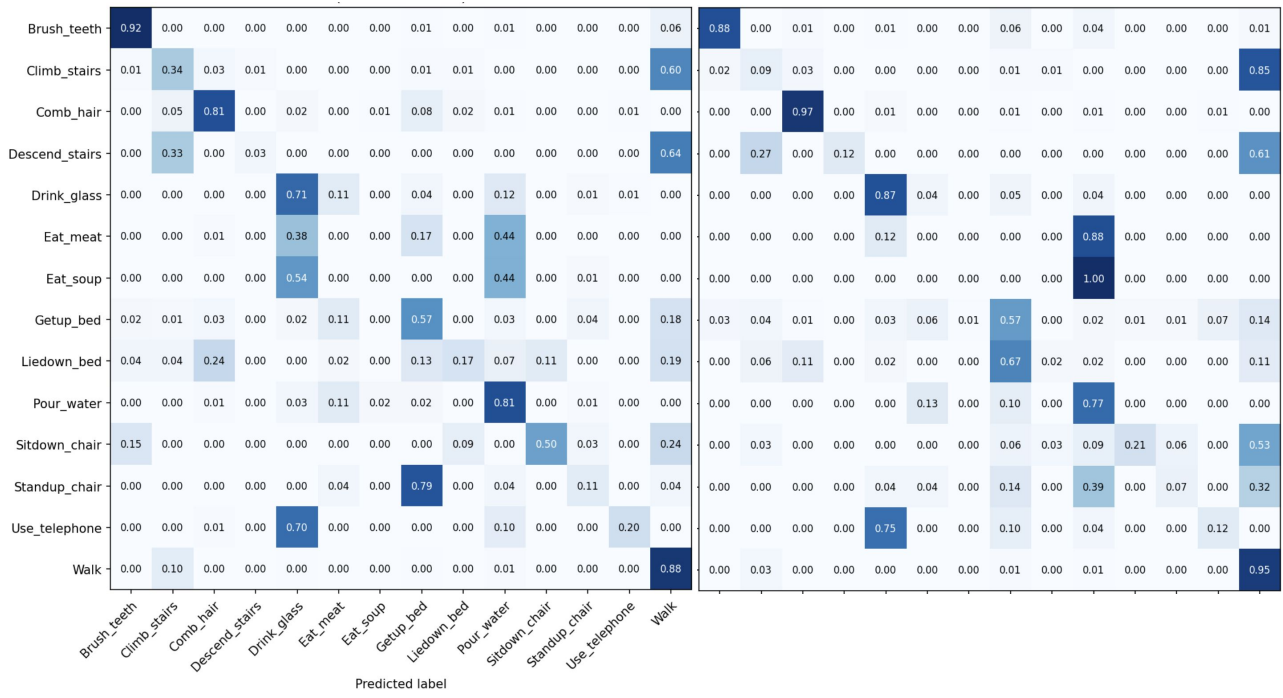


Figure 12. Bio-PM vs TF-C on WHARF.